Detection of Nanoliter-Scale Cortical Perivascular Spaces Using Heavily T_2-weighted MRI at 7T

Gael Saib[*1], Zeynep H. Demir[*1], Paul A. Taylor[2], S. Lalith Talagala[3], Alan P. Koretsky[1]

[1]Laboratory of Functional and Molecular Imaging, National Institute of Neurological Disorders and Stroke, National Institutes of Health, Bethesda, Maryland, United States, [2]Scientific and Statistical Computing Core, National Institute of Mental Health, National Institutes of Health, Maryland, United States, [3]NIH MRI Research Facility, National Institute of Neurological Disorders and Stroke, National Institutes of Health, Bethesda, Maryland, United States. *These authors contributed equally to this work.

Corresponding Author:

Gael Saib

Laboratory of Functional and Molecular Imaging, National Institute of Neurological Disorders and Stroke, National Institutes of Health

10 Center Drive, Building 10, Room B1D69

Bethesda, MD 20892, USA

email: saibgh@nih.gov

Abbreviations:

PVS: perivascular space, CSF: cerebrospinal fluid, TSE: turbo spin echo, ETL: echo train length, ES: echo spacing, FA: flip angle, BW: bandwidth, TI: inversion time, TA: acquisition time, TR: repetition time, TE: echo time, WM: white matter, GM: gray matter, CNR: CSF-to-tissue contrast to noise ratio

Abstract

Background: There is increasing interest in high-contrast cerebrospinal fluid (CSF) MRI to image perivascular spaces (PVSs). Dilated PVSs, associated with aging, dementia, and various other conditions, have been commonly detected within the white matter, basal ganglia, and midbrain. 7T MRI has enabled the early detection of smaller PVSs due to very high contrast and resolution. However, to date, PVSs in the cerebral cortex has received limited attention, despite that the identification of early changes in the cortical PVS could give valuable insight into neurological conditions.

Purpose: To determine if PVSs can be detected within the cerebral cortex in healthy participants by using heavily T_2-weighted MRI at 7T.

Materials and Methods: A T_2-weighted TSE sequence was optimized to detect CSF with high resolution and contrast at 7T while reducing the contribution from surrounding tissues. A semi-automated processing pipeline was used to extract PVSs and analyze their density in the whole brain including the cerebral cortex.

Results: A total of 17 healthy volunteers were scanned at 7T (10 Males and 7 Females, aged 40$\pm$14 years). The optimized 3D-TSE sequence (0.125 mm^3 volume, 0.5 mm isotropic resolution, 500 ms TE , 2.4 s TR and 10 min scan time) enabled a CNR of approximatively 180:1 after denoising, with a CSF volume detection limit of about 5 nL per voxel. At this sensitivity, average PVS density was found to be about 4.0% in white matter, 2.7% in deep gray matter and 1.3% in the cortex. Highest cortical PVS density was found to be in the insular cortex. Four characteristic classes of PVS morphology within the cortex or passing through the cortex were identified.

Conclusion: High-resolution CSF imaging using optimized 3D-TSE MRI at 7T allows nanoliter scale volume detection of cortical PVSs in healthy individuals. This lays the groundwork for exploring cortical PVSs and their potential for use in diagnosis or prognosis of neurological diseases.

Keywords: PVS, cerebral cortex, PVS density, PVS morphology, heavily T_2-weighted MRI, 7T, ultra-high field

1. Introduction

Perivascular spaces (PVSs), also known as Virchow-Robin spaces, are fluid-filled compartments surrounding blood vessels in the brain parenchyma (M Durand-Fardel, 1843; Virchow, 1851). They serve as a pathway of cerebrospinal fluid (CSF) flow and for exchange with interstitial fluid (ISF) that play an essential role in immune surveillance, brain homeostasis and the clearance of metabolic waste (Wardlaw et al., 2020). Emerging studies have shown that PVS dilatation is associated with aging, small vessel diseases, and neurodegenerative diseases (Francis et al., 2019). MRI has enabled the non-invasive visualization and classification of different types of PVSs according to their anatomical location in the basal ganglia, white matter (WM), and midbrain (Kwee & Kwee, 2007). More recently, PVS types were also identified in the anterior temporal lobes (McArdle et al., 2020) and hippocampus (Yao et al., 2014). Further, heavily T_2-weighted MRI at ultra-high field (≥7T) has provided superior CSF-to-tissue contrast to noise ratio (CNR) (Daoust et al., 2017; Gao et al., 2014) improving detection of PVSs at sub-millimeter resolution (Bouvy et al., 2014; Zong et al., 2016). This has allowed for the characterization and assessment of early structural changes of normal unenlarged PVSs.

Most arterial PVSs in the basal ganglia and centrum semiovale are coated with two layers of leptomeninges (Pollock et al., 1997). In the cortex, however, the membrane of smaller perforating arteries has only one single layer of leptomeninges. This membrane gets increasingly compressed by glia limitans and the pia mater against the vessel wall as the arteries branch out into smaller arterioles and capillaries (Morris et al., 2016; E. T. Zhang et al., 1990). Thus, cortical PVSs are believed to be smaller and communicating with subarachnoid CSF (Eide et al., 2018; Ringstad et al., 2018). The identification of early changes in the cortical PVS could give valuable insight into neurological conditions. In a recent postmortem study, PVS enlargement of cortical arterioles associated with cerebral amyloid angiopathy was demonstrated using high-resolution MRI (Perosa et al., 2022). To the best of our knowledge, study of cortical PVSs in the living human brain has not previously been reported, likely because of the difficulty in detection due to their small size.

In this study, a high-resolution T_2-weighted 3D Turbo Spin Echo (TSE) sequence was optimized to provide high CNR and minimal signal from parenchyma at 7T to investigate the presence of cortical PVSs in healthy individuals (Saib et al., 2023). We quantified the PVS density in the whole brain, including various cortical areas, using a semi-automated processing technique based on PVS morphology and considering local variations in background noise and signal at 7T. Further, we propose classification of PVSs exhibiting stereotypical morphology based on their locations related to intraparenchymal arteries in connection with the cortex (Akashi et al., 2017). This study lays the groundwork for assessing the diagnostic utility of

detecting cortical PVSs as well as understanding the mechanisms for structural changes in cortex for neurological disorders.

2. Materials and Methods

2.1. Study design and participants

This study was conducted under a protocol (00-N-0082) approved by the Institutional Review Board of the National Institutes of Health, Bethesda, Maryland, United States (ClinicalTrials.gov identifier: NCT 00004577). A total of 17 healthy volunteers, 10 Males and 7 Females of 40±14 years (mean±std), were recruited and signed an informed consent to participate to the study. Any participant identifiers included were not known to anyone outside the research group so it cannot be used to identify individuals. The participants were selected to ensure diversity with a broad age range of 23-67 years. All imaging was performed on a 7T Magnetom Terra (Siemens Healthineers, Erlangen, Germany) using a 1Tx-32Rx head array (Nova Medical, Wilmington, USA).

2.2. MRI acquisitions and optimization

The MRI sequence parameters used are given in Table 1. CNR of a high-resolution (0.5 mm^3 isotropic resolution) TSE sequence at 7T was optimized using different TE and ETL while restricting the scan time to ~10 min. Signal in CSF ventricles, WM, and deep gray matter (GM) was estimated using four ROIs of variable sizes drawn in a central slice. The WM and deep GM ROIs were placed in regions excluding PVSs but near the ventricles to minimize contrast variations due to non-uniform B_1 distribution at 7T. The CNR was calculated as the mean signal difference between CSF and tissue ROIs divided by the standard deviation of pixels within tissue ROIs. Numerical simulations were performed using an Extended Phase Graph algorithm (Hennig et al., 2003) (see supplementary materials). Additionally, a high-resolution T_1-weighted MP2RAGE (Marques et al., 2010) was acquired for tissue segmentation and a fluid attenuated inversion recovery (FLAIR) sequence (Hajnal et al., 1992) was performed to detect any WM hyperintensities (WMH) or lacunes.

	TSE	MP2RAGE	FLAIR
Orientation	sagittal	sagittal	sagittal
Matrix size	400 x 400 x 320	454 x 480 x 320	272 x 272 x 224
Resolution (mm^3)	0.50 x 0.50 x 0.50	0.50 x 0.50 x 0.50	0.74 x 0.74 x 0.74
FA (°)	100	5/4	Variable
TR (ms)	3400/2430	5000	9000
TE (ms)	300/500/700	1.85	273
TI (ms)	-	740/2700	2300
BW (pixel/Hz)	500	360	681
ES (ms)	4.64	7.3	3.9
ETL	151/108	264	165
GRAPPA	4	3	6
Slice partial Fourier	-	6/8	-
Elliptical scanning	yes	no	no
TA (min:sec)	10:45	14:00	10:00

Table 1: Protocol sequence parameters for 7T MRI scans conducted in this study. The CSF-to-tissue contrast to noise of TSE was assessed at three different TEs and image sharpness was evaluated at ETL 108 (~500 ms) and 151 (~700 ms). A high-resolution MP2RAGE was acquired to extract brain tissues and cortical aeras with a high accuracy. A fluid attenuated inversion recovery (FLAIR) was also performed to detect potential White Matter Hyperintensities (WMH) and lacunes that may be confounded with PVSs.

2.3. High-resolution brain segmentation and PVS processing

The framework for semi-automated processing of PVSs is summarized in Figure 1. The MP2RAGE and FLAIR images were aligned to the TSE images using a rigid transformation with *3dAllineate* in AFNI (Cox, 1996). Intra-subject TSE acquisitions were aligned using MATLAB (R2022b, MathWorks, Natick, MA, USA) affine registration tool *imregister.* MP2RAGE second inversion images were skull stripped using FSL Brain Extraction Tool (Jenkinson, M., 2005) to produce a brain mask. The brain masked T_1-weighted MP2RAGE UNI image (combined first and second inversion images) (Marques et al., 2010) was used to generate a WM mask using FSL FAST (FMRIB's Automated Segmentation Tool) (Y. Zhang et al., 2001). A flood-fill operation was performed on the WM mask to remove any imperfections arising from large WM PVSs mistaken as GM tissue during segmentation. The heavily T_2-weighted TSE images were denoised by applying a block-matching 4D filtering (BM4D) (Maggioni et al., 2013). A bulk CSF mask was extracted from the denoised TSE images by adaptive thresholding using the MATLAB function

adaptthresh with a cubic neighborhood of 35 voxels and selection of largest connected cluster with MATLAB function *bwconncomp.* Dilatation of 1 voxel was applied to the CSF mask to exclude any residual partial voluming of bulk CSF signal with tissue. The GM mask was generated by extracting the region between the WM and CSF masks. Additionally, a multi-modal cortical parcellation atlas with 180 areas per hemisphere (Glasser et al., 2016) was aligned to MP2RAGE UNI images and refined using AFNI's *3dROIMaker* and *3dcalc* to ensure ROI boundaries after mapping were constrained within the subject's GM mask and that resampling left no gaps among ROIs. The separation of the cortex and deep GM was performed by subtracting the atlas region from the GM mask.

PVS mapping consisted of calculating the Z-scores in each vessel-like structure detected in the denoised TSE images based on their local noise in a surrounding region. The vesselness of each voxel was estimated by 3D Frangi filtering (Frangi et al., 1998) using default parameters ($\propto$=0.5, β=0.5, c=500). The Frangi filter scale was set to a large range of 1 to 11 voxels with a step size of 1 voxel to maximize the inclusion of potentially very small PVSs. A 2 mm spherical region surrounding each potential PVSs excluding any other vessel-like structures overlapping within this region was defined to estimate the local noise. The local Z-score was calculated as the signal difference between the potential PVS signal and the mean signal of the surrounding region divided by the standard deviation of the signal in the surrounding region. The Z-score map was thresholded at 2.58, equivalent to a 99.5% confidence (1-sided) that the voxel PVS signal was above the mean local noise. Finally, the resulting PVS maps underwent a manual correction to remove potential WMH, lacunes or remaining bulk CSF not excluded by the Frangi filter or the CSF mask.

The PVS density was calculated as the total number of voxels with a Z>2.58 divided by the total number of voxels in the WM, deep GM, and cortical GM masks (%) excluding the region below the top of cerebellum commonly affected by signal reduction due to the use of head arrays at 7T. Scan-rescan data were acquired in 7 subjects within the same session without repositioning in the magnet. The reproducibility of PVS density measurements was assessed by calculating intraclass coefficients (ICC) using one-way random effects model (1,1) and by Bland-Altman analysis. Subsequently, the PVS density was also quantified in 266 cortical areas of the brain atlas within the brain region selected for analysis.

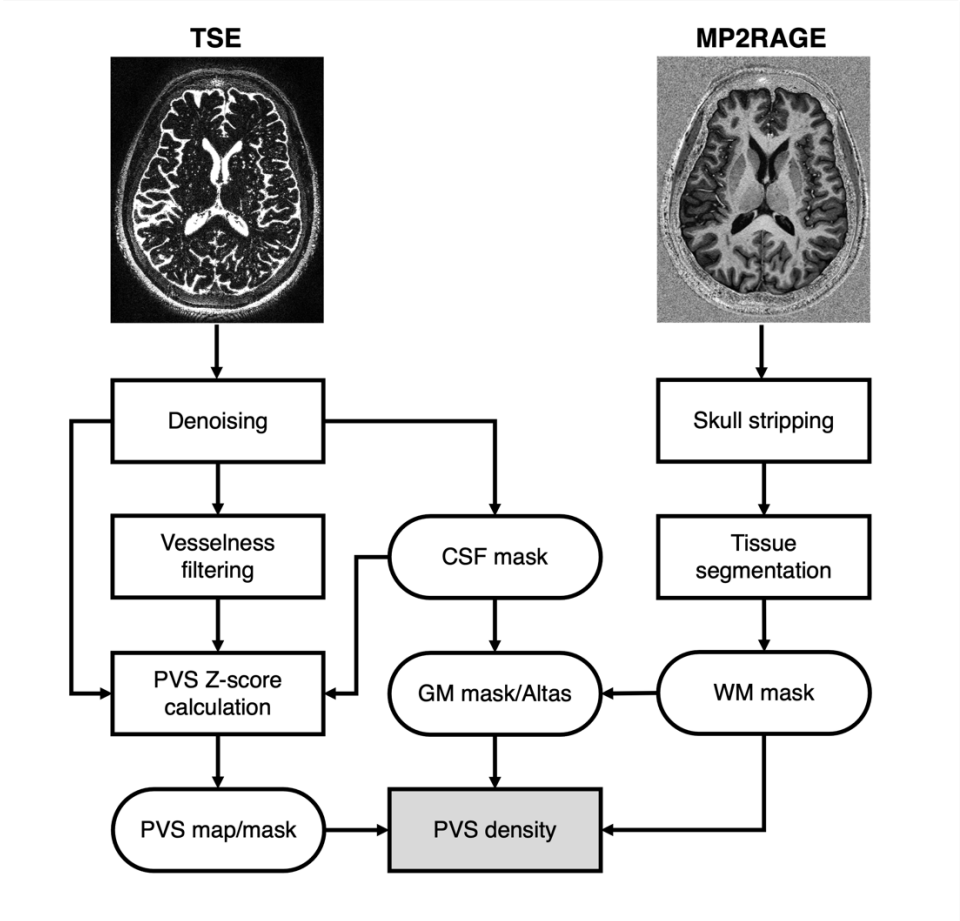

Figure 1: Flow chart of semi-automated perivascular space (PVS) processing. PVS extraction consisted of applying a vesselness Frangi filter to the denoised TSE images to calculate a Z-score map of each vesselness structures based on their average surrounding noise. In addition, the TSE images were used to extract a bulk cerebrospinal fluid (CSF) mask while skull stripping and white matter (WM) segmentation was conducted on MP2RAGE high-resolution anatomical images with FSL. Gray matter (GM) mask was generated by extracting the region between WM and bulk CSF masks. A cortical atlas was then generated using GM mask. PVS density was calculated by the ratio of PVS voxels detected with a Z-score > 2.58 in tissue mask divided by the total number of voxels in tissue mask.

3. Results

3.1. TSE contrast optimization for PVS detection at 7T

Figure 2A shows heavily T_2-weighted TSE images acquired at different TE values for a representative subject. CSF-filled PVSs can be identified as bright punctual or tubular structures depending on their orientation in the images. As predicted from simulations (Fig S1A), TSE images acquired at TEs

of 500 and 700 ms show high CSF signal against a very low background signal. Measured CNR (~100:1) was optimal for both WM and GM at TE = 500 ms (Fig 2B). Maximum intensity projection (MIP) of these images shows elongated features that are PVSs (Fig 2C). Use of a protocol with a shorter ETL improved the overall image sharpness, allowing better depiction of small PVS. CNR with shorter ETL of 108 was reduced to 54:1 due to the use of a shorter TR required to maintain scan time under 10 min as expected from simulations (Fig S1). Denoised TSE images resulted in a CNR of 180:1 with a CSF signal intensity 40 times higher than mean background tissue signal. The average CSF signal within the ventricles was found to be 330±51 across subjects. Using a threshold of 2.58 standard deviations above the mean of background signal (8.3±1.8, mean±std), this MRI protocol allows the detection of CSF volumes of about 5 nL per voxel (125 nL*12.9/330).

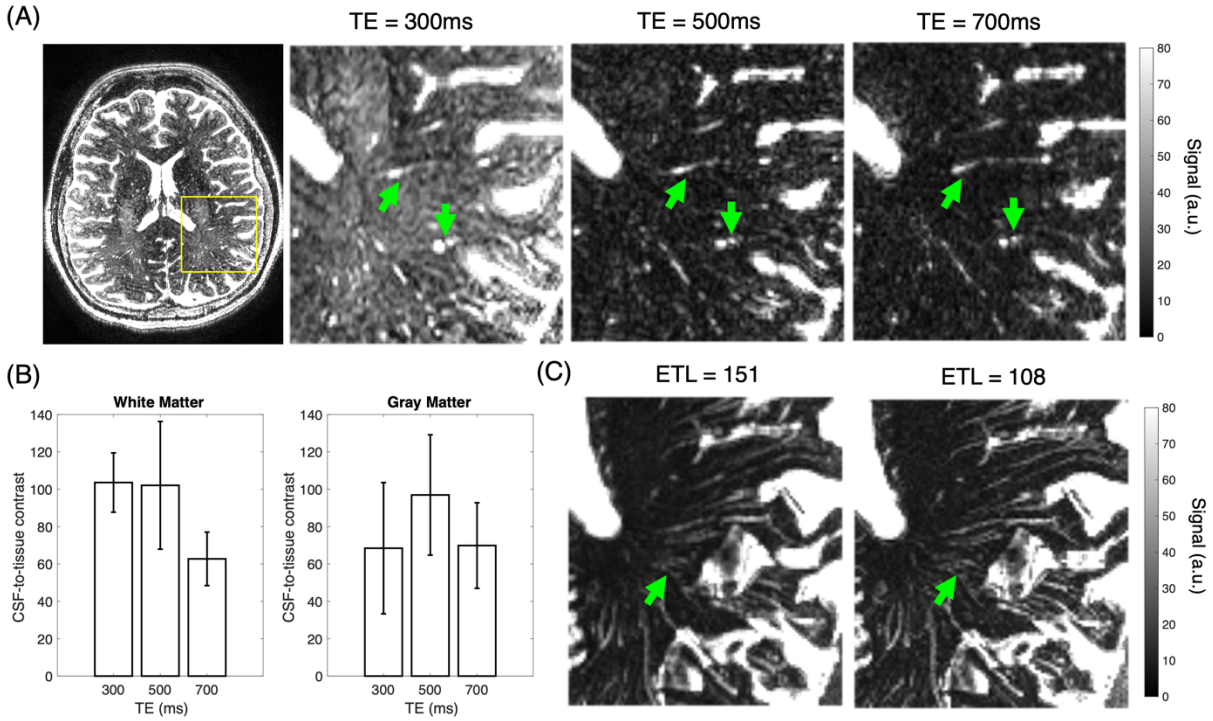

Figure 2: TSE optimization with (A) TSE images acquired at different effective TEs in a representative subject and (B) corresponding mean CNR contrasts determined from four subjects. PVS can be depicted as bright punctual and linear structures as pointed by the green arrows. Note that the contrast is optimal at TE = 500 ms for both the WM and GM. (C) Comparison of 5.5 mm MIP of TSE images (TE = 500 ms) acquired with a ETL of 151 (TR = 3.4 s) and 108 (TR = 2.4 s). PVS can be identified as linear structures with high signal intensity. Use of a reduced ETL improved the visualization of small PVS as pointed by the green arrows.

3.2. ,Whole-brain semi-automated PVS quantification

Figure 3 shows an example of PVS maps, and associated Z-score maps processed by the framework presented in Figure 1. As expected, it can be seen that the axial PVS maps along with their corresponding Z-score maps are similar. Elongated structures appear best at increasing MIP thickness, revealing typical tubular features of PVSs. The highest Z-scores were found prominently within the basal ganglia and WM centrum semiovale. PVS Z-score exhibited values as high as 114±63 across subjects. However, mean Z-score of PVSs above the threshold of Z=2.58 was 6±1. Z-scores close to CNR measured in ventricles were likely associated with large PVS while lower Z-scores were attributed to partial volume effects of small PVSs and large PVS edges voxels with surrounding tissue.

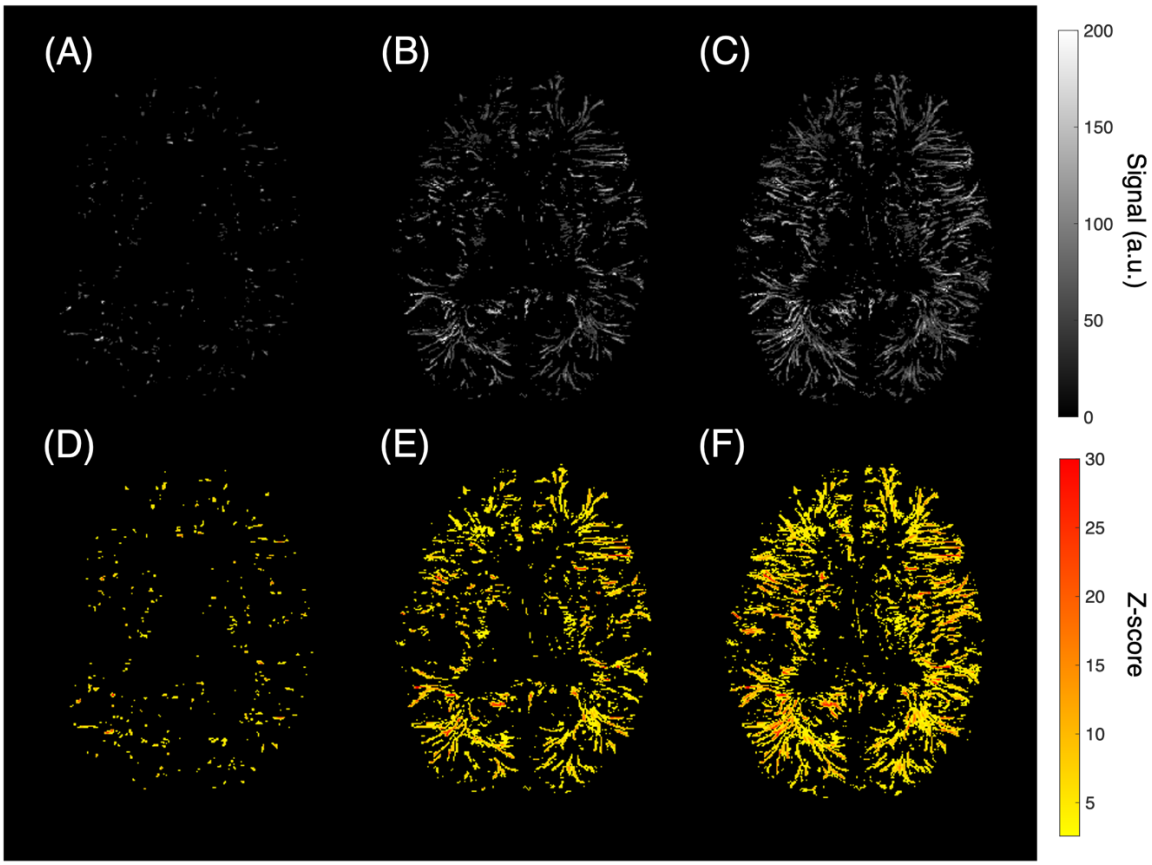

Figure 3: Example of perivascular space (PVS) map with associated Z-score map of a representative subject. (A-C) PVS maps display extracted TSE signal and (D-F) thresholded (2.58) Z-scores maps corresponding to A-C. (A) and (D) axial slice at the level of the ventricles (B) and (E) 3 mm-MIP and (C) and (F) 5.5 mm-MIP. PVS structures with elevated signal intensity in the TSE image exhibit high Z-score values that are likely corresponding to large PVS, more prominently seen in the basal ganglia and WM.

3.3. Cortical PVS can be detected throughout the brain

A significant number of PVSs were detected in various cortical areas, as illustrated by the examples in Figure 4. Highest Z-scores of cortical PVSs were found to be 69±16 across subjects, more frequently near the insula and piriform (Fig 4A). The TSE signal intensity profile in these regions shows signal intensity peaks that correspond to PVS Z-score above 2.58. Lower signal intensity peaks with a Z-score near chosen threshold (Z=2.58) were also detected that confirms our ability to extract PVS signal in this region as well as in distal cortical aeras (Fig 4B). Some peaks in intensity may not be visible in the Z-score map, either because they were below our threshold or not detected by the Frangi filter. Similarly to WM, the mean PVS Z-score in the cortex was found to be 5.8±2.

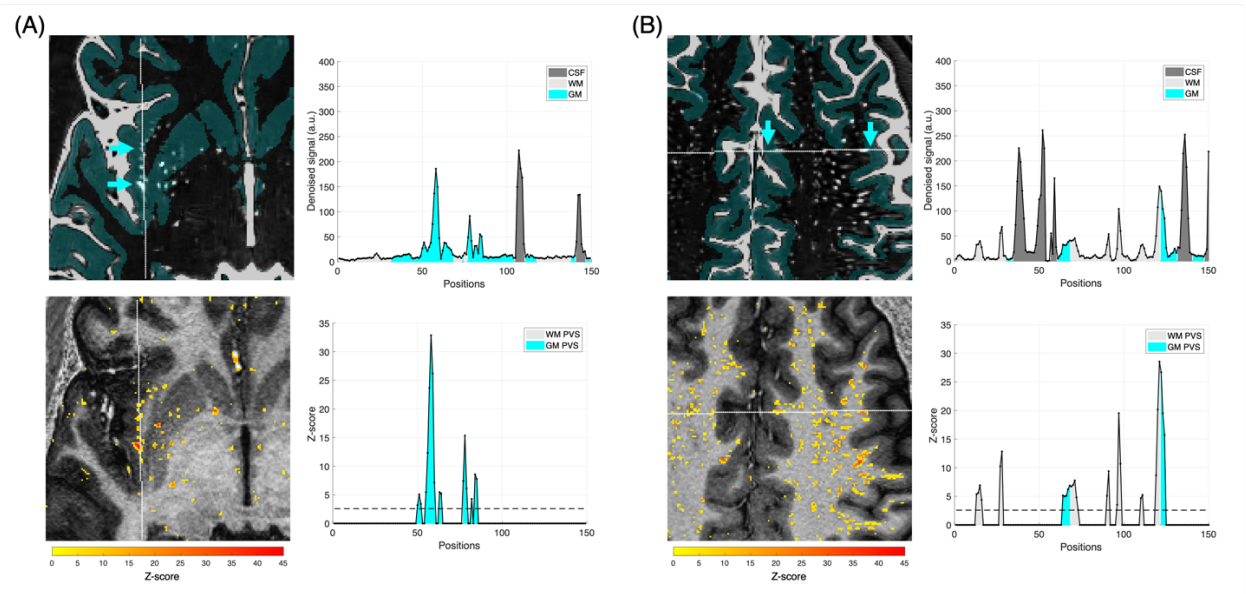

Figure 4: Perivascular space (PVS) detection with line intensity profiles and associated Z-scores. Examples of cortical PVSs were detected within the GM mask (highlighted in cyan) in TSE images in two representative subjects. The line intensity profiles along white lines across the TSE images and Z-score maps are passing through cortical PVS (pointed by arrows in TSE) within (A) the insular/piriform cortex and (B) a distal cortical aera. The top graphs indicate high signal intensity peaks that correspond to bulk CSF and PVSs in TSE signal while the bottom graphs show corresponding extracted PVS Z-scores. An example of large cortical PVSs exhibiting a high Z-score (Z>30) is shown in (A) with other smaller cortical PVSs at lower Z-scores. Two PVSs crossing the WM-cortical boundary are shown in (B) with multiple WM PVSs. Note that signal intensity peaks not detected in Z-score graphs were not extracted by the Frangi vesselness filter or below Z=2.58 (dotted line).

Figure 5 illustrates four types of PVS morphologies typically observed in cortex from the large majority of subjects. Three types were likely associated with intracortical, medullary and juxtacortical arteries. Figure 5A shows an example of an intracortical PVS, which likely surround small vessels inside the cortex without apparent extension to the WM. Figure 5B illustrates a PVS with a portion extending into both WM and cortex possibly associated with medullary arteries. None of these PVSs were found to connect directly with the subarachnoid space. The detection of PVSs near this region may be challenging since bulk CSF was dilated by 1 voxel to avoid errors due to partial volume effects. Figure 5C presents an example of a third type of PVS that ended within the juxtacortical at the WM-GM border. Finally, Figure 5D portrays a fourth PVS morphology that was frequently observed. These were group of PVSs, appearing as clusters arranged in a 'brush' or 'flower' shape, generally located near the WM-cortical boundary or within the cortex. The location of these PVS clusters vary from subject to subject, but they frequently appear near the piriform and insular cortex (see Fig S2-S4 for more examples). Moreover, these clusters can be so dense that the CSF content tends to decrease WM signal intensity in T_1-weighted acquisitions which can affect WM differentiation near the GM (Fig S5).

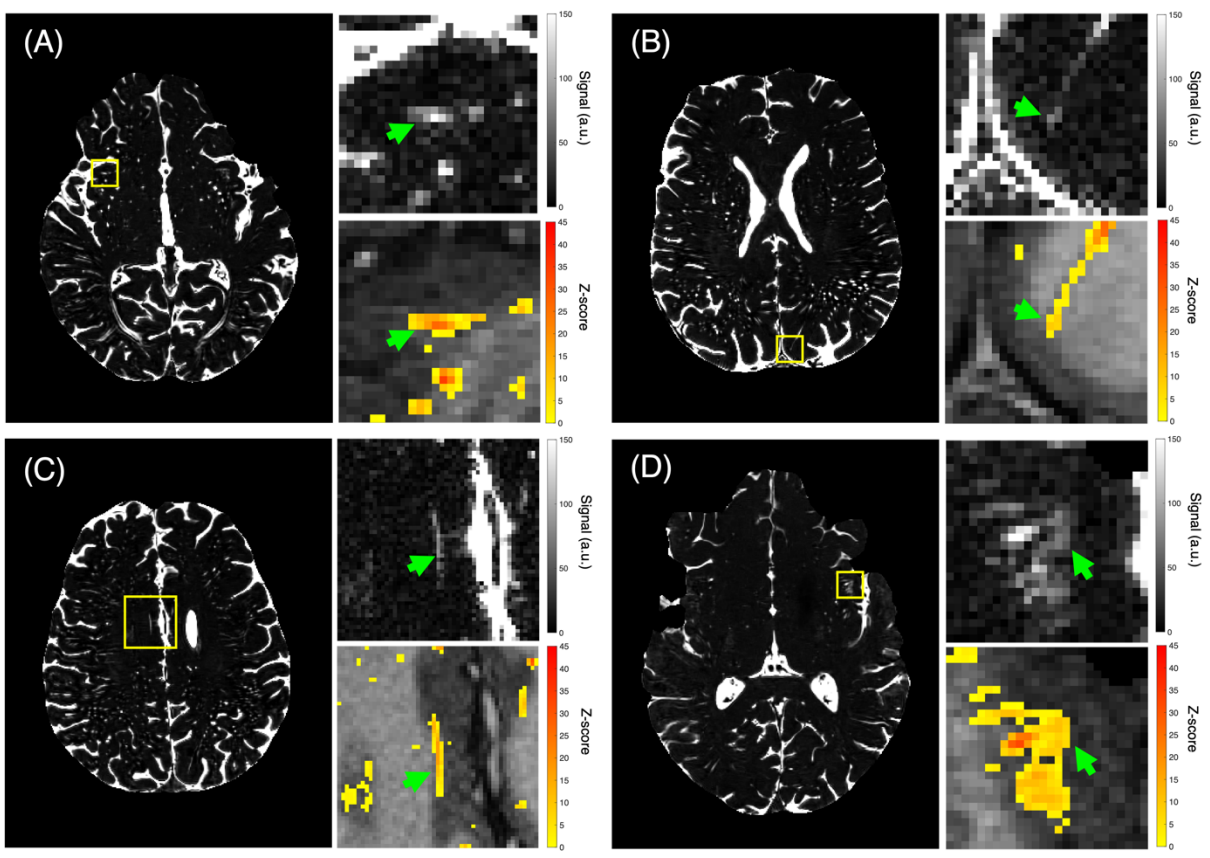

Figure 5: Representative examples of cortical perivascular space (PVS) morphology observed in most subjects with (A) intracortical PVS located inside the cortex not extending into WM, (B) Medullary PVS

extending between the WM and cortex, (C) juxtacortical PVS following the WM-GM boundary and (D) cluster of small PVS arranged in 'flowers' within the cortex and juxtacortical area. For each type, the green arrows are pointing the portion of PVS detected inside the cortex.

3.4. *PVS density in WM, Deep GM, and cortex*

The PVS density measured in WM, deep GM, and cortex across the 17 subjects is shown in Figure 6A. The density was calculated as the number of PVS voxels above Z=2.58 divided by number of voxels in each tissue type. The average PVS density was found to be 4±1% in WM, 2.7±1.5% in the deep GM and 1.3±0.3% in the cortex. As expected, the density of cortical PVSs were lower than WM or deep GM PVS densities. The scan-rescan reliability shows a good intrasubject reproducibility of repeated PVS measurement with an ICC of 0.94, 0.97, and 0.78 respectively for WM, deep GM, and cortex (Fig 5B). The 95% limit of agreement in Bland-Altman analysis was exceeded for one subject in the WM and deep GM, likely due to motion artifacts in the rescan TSE acquisition. The PVS density was quantified in 266 specific cortical areas above the cerebellum. Figure 6C shows the top twenty cortical density regions with the highest being the Anterior Agranular Insula Complex (AAIC) and the Posterior Insular Area (PoI1, PoI2) with a range of ~3.9-7.5% probably linked to branches of the Middle Cerebral Arteries (MCA). The areas with some of the lowest densities were found at a range of ~0.2-0.5% primarily in the Primary Auditory cortex (A1) and the Medial Belt Complex (MBelt). Table S1 summarizes all regional PVS densities of the 266 cortical areas averaged across the participants.

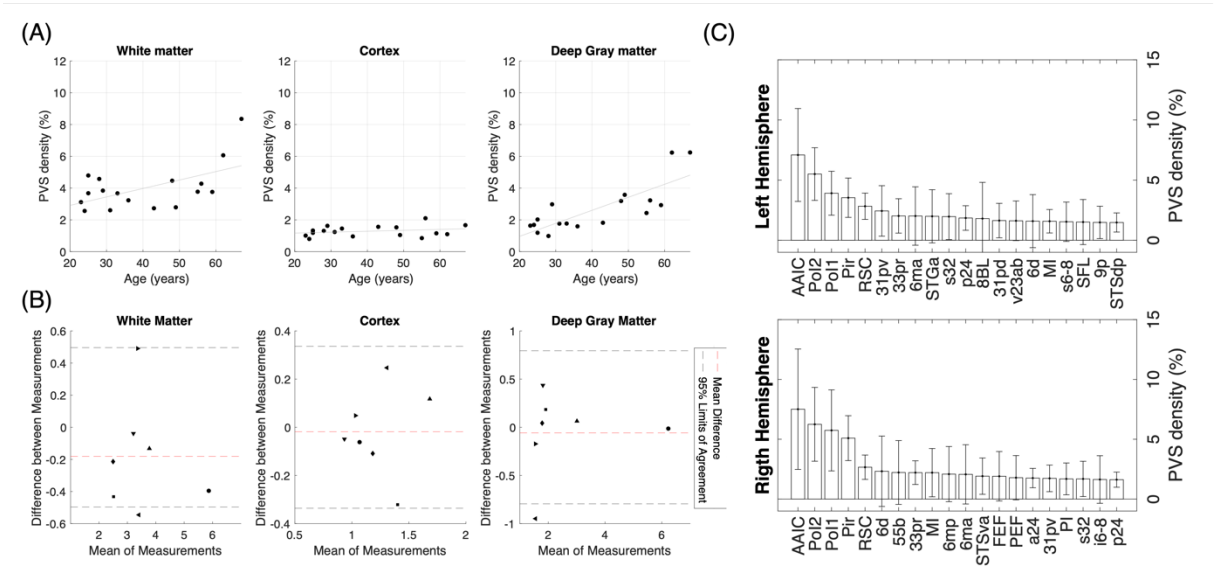

Figure 6: Perivascular space (PVS) quantification with (A) PVS density extracted in the 17 subjects within WM, cortex, deep GM and (B) Bland-Altman analysis showing the reproducibility of PVS density measurements in these regions for 7 subjects. The black dotted lines represent 95% interval of confidence while the red dotted line shows the mean of the difference between scan and rescan measurements for each subject. Note that the differences in density found between the scans and rescans slightly exceeded 95% confidence interval in the WM and deep GM for one subject. Cortical PVS density was calculated in 266 atlas regions as shown in (C) with 20 highest densities in both hemispheres. Highest PVS density (~4-8%) was found in Anterior Agranular Insula Complex (AAIC) and Posterior Insular Area (PoI1, PoI2) while lowest (< 0.5%) were found in Primary Auditory cortex (A1) and the Medial Belt Complex (MBelt).

4. Discussion

This study presents an optimized T_2-weighted 3D-TSE sequence that enhances CSF contrast at 7T enabling the detection of cortical PVSs in healthy individuals. Many PVSs found within the cortex had signal consistent with a sub-voxel volume. Brain tissue suppression with TSE was excellent at TE=500 ms using a constant flip angle of 100° and TR of 2.4 s. Employing a reduced ETL and flip angle resulted in lower the echo signal variation across the ETL, leading to minimal blurring as well as lower SAR. In this work, a very high CNR of 180:1 was achieved allowing PVS volume detection of about 5 nanoliters within a 0.125 mm^3 voxel with 99.5 % confidence. CSF-to-tissue signal intensity ratio was ~4 times lower than simulated ratio likely due to remaining physiological noise contributing to the tissue signal. Further improvements will be possible by minimizing background tissue noise further and adding motion correction techniques.

Several types of PVSs have been classified in the literature based on their anatomical locations, primarily related to vessels in the basal ganglia, the subcortical WM, the midbrain regions (Kwee & Kwee, 2007) and the anterior temporal lobes (McArdle et al., 2020). In analogy, we described four types of PVSs based on their morphological appearances at achievable sensitivity that are likely related to cortical perforating arteries. The first three types of PVS were classified according to the location of PVSs relative to the cortex, likely following the intracortical, subcortical, and medullary arteries (Akashi et al., 2017). At our detection level, we found that some cortical PVSs stayed entirely within the cortex (classified as intracortical), some ended right at the juxtacortical boundary within WM (classified as subcortical), and some could be traced through the cortex extending to WM (classified as medullary). This latter type may be similar to subcortical WM PVSs previously classified in the literature as type II (Kwee & Kwee, 2007). The fourth type of cortical PVSs were organized in dense clusters with a unique morphology that started at

the GM-WM subcortical region. These PVS clusters appeared in different anatomical locations, but most were notably found near the insula and piriform regions. This is likely due to several cortical vessels coming together into a single WM vessel. In some cases, the clusters were dense enough to alter the apparent signal of WM in MP2RAGE images affecting the definition of the GM-WM cortical boundary. Aligning cortical PVSs to high resolution angiography will provide a better understanding of the association of these PVS types with the underlying cerebral vasculature.

The semi-automated processing method developed in this study relies on the vesselness extraction and mapping of PVS local Z-score. This accounts for spatial noise variation well known to be prominent at 7T (Triantafyllou et al., 2005) and does not require specific parametrization of Frangi filtering and subsequent thresholding. The brain MRI alignment and segmentation pipeline allowed for the extraction of bulk CSF, WM, and GM as well as the definition of 266 cortical areas for the quantification of the PVS densities. Unfortunately, segmentation was unable to separate the thalamus from WM and hence it was included in that tissue mask due to the poor contrast of the 7T MP2RAGE images in this region. MRI contrast may be improved with parallel transmission RF pulses at 7T (Gras et al., 2017). This should also help minimizing TSE contrast variation for volumetric PVS mapping. Since, the signal intensity of 100 % CSF voxel corresponds to a voxel volume of 125 nL (0.125 mm^3), the volume of each PVS in the thresholded Z-score map could be deduced by scaling the voxel volume by the ratio of signal inside PVS and CSF signal.

The average PVS density was found to be ~4.0 % and 2.7 % respectively in WM and deep GM PVS across subjects. The WM density measured is with the range reported in a previous studies (Barisano et al., 2021; Cai et al., 2015). The PVS density was about ~1.3% in the cortex which was, as expected, much lower compared to WM density. The highest PVS density was found in the insular cortex (AAIC, PoI1 and PoI2). The insular cortex is supplied by perforated branches from M2 branches of the MCA, which may involve larger arteries and PVSs compared to penetrating vessels in other cortical aeras (Varnavas & Grand, 1999). The lowest PVS density was found in the auditory cortex (MBelt and A1). Most studies concur that PVS volume and frequency in the centrum semiovale, basal ganglia and hippocampus tend to increase with age. Although there was an increase of the PVS density within WM and deep GM with age, the cortical PVS density was found to be similar among all individuals. A larger group will be necessary to assess if cortical PVS volume changes with aging. It is known that the inter-subject variability in the WM and deep GM is large since the PVS density has been found to rely on multiple factors even in the healthy population (Barisano et al., 2021).

In conclusion, PVSs were extracted with a CSF-to-tissue contrast to noise of ~180:1 resulting in 5 nano-liter volume detection within 0.125 mm^3 voxels using an optimized T_2-weighted 3D-TSE at 7T. Four

distinct morphologies of cortical PVSs were consistently identified in healthy individuals. This work opens up the use of imaging to assess changes in cortical PVSs that could help to characterize various neurological conditions.

Data and Code availability

Data are available on https://figshare.com at dx.doi.org/10.6084/m9.figshare.26671444.

Author Contributions

GS and ZHD have equal first authorship. ZHD conceived of the presented idea and developed the theory, as well as leading subject recruitment. GS performed technical design, optimizing MRI sequences and managing the majority of the data processing. GS conducted the experiments and data acquisitions with ZHD. GS and ZHD analyzed and interpreted the data together. GS wrote the manuscript, with contributions from ZHD. P.A.T handled MRI image alignments and provided input on technical aspects. S.L.T contributed to data analysis and the writing of the manuscript. A.P.K provided insights on study design and data processing, supervised the project and contributed to the manuscript.

Funding

This research was supported by the Intramural Research Program of the National Institute of Neurological Disorders and Stroke at the National Institutes of Health.

Declaration of Competing Interests

All authors declare that no competing interest exist.

References

Akashi, T., Takahashi, S., Mugikura, S., Sato, S., Murata, T., Umetsu, A., & Takase, K. (2017). Ischemic White Matter Lesions Associated With Medullary Arteries: Classification of MRI Findings Based on the Anatomic Arterial Distributions. *American Journal of Roentgenology*, *209*(3), W160–W168. https://doi.org/10.2214/AJR.16.17231

Barisano, G., Sheikh-Bahaei, N., Law, M., Toga, A. W., & Sepehrband, F. (2021). Body mass index, time of day and genetics affect perivascular spaces in the white matter. *Journal of Cerebral Blood Flow & Metabolism*, *41*(7), 1563–1578. https://doi.org/10.1177/0271678X20972856

Bouvy, W. H., Biessels, G. J., Kuijf, H. J., Kappelle, L. J., Luijten, P. R., & Zwanenburg, J. J. M. (2014). Visualization of Perivascular Spaces and Perforating Arteries With 7 T Magnetic Resonance Imaging: *Investigative Radiology*, *49*(5), 307–313. https://doi.org/10.1097/RLI.0000000000000027

Cai, K., Tain, R., Das, S., Damen, F. C., Sui, Y., Valyi-Nagy, T., Elliott, M. A., & Zhou, X. J. (2015). The feasibility of quantitative MRI of perivascular spaces at 7 T. *Journal of Neuroscience Methods*, *256*, 151–156. https://doi.org/10.1016/j.jneumeth.2015.09.001

Cox, R. W. (1996). AFNI: Software for Analysis and Visualization of Functional Magnetic Resonance Neuroimages. *Computers and Biomedical Research*, *29*(3), 162–173. https://doi.org/10.1006/cbmr.1996.0014

Daoust, A., Dodd, S., Nair, G., Bouraoud, N., Jacobson, S., Walbridge, S., Reich, D. S., & Koretsky, A. (2017). Transverse relaxation of cerebrospinal fluid depends on glucose concentration. *Magnetic Resonance Imaging*, *44*, 72–81. https://doi.org/10.1016/j.mri.2017.08.001

Eide, P. K., Vatnehol, S. A. S., Emblem, K. E., & Ringstad, G. (2018). Magnetic resonance imaging provides evidence of glymphatic drainage from human brain to cervical lymph nodes. *Scientific Reports*, *8*(1), 7194. https://doi.org/10.1038/s41598-018-25666-4

Francis, F., Ballerini, L., & Wardlaw, J. M. (2019). Perivascular spaces and their associations with risk factors, clinical disorders and neuroimaging features: A systematic review and meta-analysis. *International Journal of Stroke*, *14*(4), 359–371. https://doi.org/10.1177/1747493019830321

Frangi, A. F., Niessen, W. J., Vincken, K. L., & Viergever, M. A. (1998). Multiscale vessel enhancement filtering. In W. M. Wells, A. Colchester, & S. Delp (Eds.), *Medical Image Computing and Computer-Assisted Intervention—MICCAI'98* (Vol. 1496, pp. 130–137). Springer Berlin Heidelberg. https://doi.org/10.1007/BFb0056195

Gao, K. C., Nair, G., Cortese, I. C. M., Koretsky, A., & Reich, D. S. (2014). Sub-millimeter imaging of brain-free water for rapid volume assessment in atrophic brains. *NeuroImage*, *100*, 370–378. https://doi.org/10.1016/j.neuroimage.2014.06.014

Glasser, M. F., Coalson, T. S., Robinson, E. C., Hacker, C. D., Harwell, J., Yacoub, E., Ugurbil, K., Andersson, J., Beckmann, C. F., Jenkinson, M., Smith, S. M., & Van Essen, D. C. (2016). A multi-modal parcellation of human cerebral cortex. *Nature*, *536*(7615), 171–178. https://doi.org/10.1038/nature18933

Gras, V., Vignaud, A., Amadon, A., Bihan, D., & Boulant, N. (2017). Universal pulses: A new concept for calibration-free parallel transmission. *Magnetic Resonance in Medicine*, *77*(2), 635–643. https://doi.org/10.1002/mrm.26148

Hajnal, J. V., Coene, B. D., Lewis, P. D., Baudouin, C. J., Cowan, F. M., Pennock, J. M., Young, I. R., & Bydder, G. M. (1992). High Signal Regions in Normal White Matter Shown by Heavily T2-Weighted CSF Nulled IR Sequences: *Journal of Computer Assisted Tomography*, *16*(4), 506–513. https://doi.org/10.1097/00004728-199207000-00002

Hennig, J., Weigel, M., & Scheffler, K. (2003). Multiecho sequences with variable refocusing flip angles: Optimization of signal behavior using smooth transitions between pseudo steady states (TRAPS). *Magnetic Resonance in Medicine*, *49*(3), 527–535. https://doi.org/10.1002/mrm.10391

Jenkinson, M. (2005). *BET2: MR-based estimation of brain, skull and scalp surfaces*. Eleventh Annual Meeting of the Organization for Human Brain Mapping.

Kwee, R. M., & Kwee, T. C. (2007). Virchow-Robin Spaces at MR Imaging. *RadioGraphics*, *27*(4), 1071–1086. https://doi.org/10.1148/rg.274065722

M Durand-Fardel. (1843). *Traité du ramollissement du cerveau*.

Maggioni, M., Katkovnik, V., Egiazarian, K., & Foi, A. (2013). Nonlocal Transform-Domain Filter for Volumetric Data Denoising and Reconstruction. *IEEE Transactions on Image Processing*, *22*(1), 119–133. https://doi.org/10.1109/TIP.2012.2210725

Marques, J. P., Kober, T., Krueger, G., Van Der Zwaag, W., Van De Moortele, P.-F., & Gruetter, R. (2010). MP2RAGE, a self bias-field corrected sequence for improved segmentation and T1-mapping at high field. *NeuroImage*, *49*(2), 1271–1281. https://doi.org/10.1016/j.neuroimage.2009.10.002

McArdle, D. J. T., Lovell, T. J. H., Lekgabe, E., & Gaillard, F. (2020). Opercular perivascular cysts: A proposed new subtype of dilated perivascular spaces. *European Journal of Radiology*, *124*, 108838. https://doi.org/10.1016/j.ejrad.2020.108838

Morris, A. W. J., Sharp, M. M., Albargothy, N. J., Fernandes, R., Hawkes, C. A., Verma, A., Weller, R. O., & Carare, R. O. (2016). Vascular basement membranes as pathways for the passage of fluid into and out of the brain. *Acta Neuropathologica*, *131*(5), 725–736. https://doi.org/10.1007/s00401-016-1555-z

Perosa, V., Oltmer, J., Munting, L. P., Freeze, W. M., Auger, C. A., Scherlek, A. A., Van Der Kouwe, A. J., Iglesias, J. E., Atzeni, A., Bacskai, B. J., Viswanathan, A., Frosch, M. P., Greenberg, S. M., & Van Veluw, S. J. (2022). Perivascular space dilation is associated with vascular amyloid-β accumulation in the overlying cortex. *Acta Neuropathologica*, *143*(3), 331–348. https://doi.org/10.1007/s00401-021-02393-1

Pollock, H., Hutchings, M., Weller, R. O., & Zhang, E.-T. (1997). Perivascular spaces in the basal ganglia of the human brain: Their relationship to lacunes. *Journal of Anatomy*, *191*(3), 337–346. https://doi.org/10.1046/j.1469-7580.1997.19130337.x

Ringstad, G., Valnes, L. M., Dale, A. M., Pripp, A. H., Vatnehol, S.-A. S., Emblem, K. E., Mardal, K.-A., & Eide, P. K. (2018). Brain-wide glymphatic enhancement and clearance in humans assessed with MRI. *JCI Insight*, *3*(13), e121537. https://doi.org/10.1172/jci.insight.121537

Saib, G., Demir, Z., Taylor, P. A., Talagala, L. S., & Koretsky, A. P. (2023). Visualization of Perivascular Spaces using an Optimized 3D-TSE sequence with Reduced Flip Angle at 7T. *Proceedings of the Annual Meeting of ISMRM*.

Triantafyllou, C., Hoge, R. D., Krueger, G., Wiggins, C. J., Potthast, A., Wiggins, G. C., & Wald, L. L. (2005). Comparison of physiological noise at 1.5 T, 3 T and 7 T and optimization of fMRI

acquisition parameters. *NeuroImage*, *26*(1), 243–250. https://doi.org/10.1016/j.neuroimage.2005.01.007

Varnavas, G. G., & Grand, W. (1999). The Insular Cortex: Morphological and Vascular Anatomic Characteristics. *Neurosurgery*, *44*(1), 127–136. https://doi.org/10.1097/00006123-199901000-00079

Virchow, R. (1851). Ueber die Erweiterung kleinerer Gefäfse: Hierzu Tab. IV. *Archiv für Pathologische Anatomie und Physiologie und für Klinische Medicin*, *3*(3), 427–462. https://doi.org/10.1007/BF01960918

Wardlaw, J. M., Benveniste, H., Nedergaard, M., Zlokovic, B. V., Mestre, H., Lee, H., Doubal, F. N., Brown, R., Ramirez, J., MacIntosh, B. J., Tannenbaum, A., Ballerini, L., Rungta, R. L., Boido, D., Sweeney, M., Montagne, A., Charpak, S., Joutel, A., Smith, K. J., … colleagues from the Fondation Leducq Transatlantic Network of Excellence on the Role of the Perivascular Space in Cerebral Small Vessel Disease. (2020). Perivascular spaces in the brain: Anatomy, physiology and pathology. *Nature Reviews Neurology*, *16*(3), 137–153. https://doi.org/10.1038/s41582-020-0312-z

Yao, M., Zhu, Y.-C., Soumaré, A., Dufouil, C., Mazoyer, B., Tzourio, C., & Chabriat, H. (2014). Hippocampal perivascular spaces are related to aging and blood pressure but not to cognition. *Neurobiology of Aging*, *35*(9), 2118–2125. https://doi.org/10.1016/j.neurobiolaging.2014.03.021

Zhang, E. T., Inman, C. B., & Weller, R. O. (1990). Interrelationships of the pia mater and the perivascular (Virchow-Robin) spaces in the human cerebrum. *Journal of Anatomy*, *170*, 111–123.

Zhang, Y., Brady, M., & Smith, S. (2001). Segmentation of brain MR images through a hidden Markov random field model and the expectation-maximization algorithm. *IEEE Transactions on Medical Imaging*, *20*(1), 45–57. https://doi.org/10.1109/42.906424

Zong, X., Park, S. H., Shen, D., & Lin, W. (2016). Visualization of perivascular spaces in the human brain at 7 T: Sequence optimization and morphology characterization. *NeuroImage*, *125*, 895–902. https://doi.org/10.1016/j.neuroimage.2015.10.078